# ADVANCED ENERGY MATERIALS

# Supporting Information

## Air-Degradation Mechanisms in Mixed Lead-Tin Halide Perovskites for Solar Cells

*Vincent J.-Y. Lim, Aleksander M. Ulatowski, Christina Kamaraki, Matthew T. Klug, Laura Miranda Perez, Michael B. Johnston, and Laura M. Herz\**

# Supporting Information

**Title: Air-Degradation Mechanisms in Mixed Lead-Tin Halide Perovskites for Solar Cells**

*Vincent J.-Y. Lim, Aleksander M. Ulatowski, Christina Kamaraki, Matthew T. Klug, Laura Miranda Perez, Michael B. Johnston, Laura M. Herz\**

## 1. Sample Fabrication

We fabricated $FA_{0.75}Cs_{0.25}Pb_{0.5}Sn_{0.5}I_3$ (mixed lead-tin) and $FA_{0.75}Cs_{0.25}SnI_3$ (tin-only) metal-halide perovskite thin films for the investigations presented in the main text. The choice of the A-cation composition ($FA_{0.75}Cs_{0.25}$) was made because of its relevance to photovoltaic device applications owing to the long term stability this composition provides.[1] We further examined $FA_{0.6}MA_{0.4}Pb_{0.5}Sn_{0.5}I_3$ to eliminate any effects of A-cation as shown in Section 0.[2]

### 1.1 Materials

Lead (II) iodide ($PbI_2$, ultra-dry, 99.999% mesh beads), tin (II) iodide ($SnI_2$, ultra-dry, 99.999% mesh beads), were purchased from Alfa Aesar. Cesium iodide (CsI, 99.9%), N,N-dimethylformamide (DMF, anhydrous), dimethyl sulfoxide (DMSO, anhydrous) and anisole (anhydrous) were sourced from Sigma Aldrich. Tin (II) fluoride ($SnF_2$, 99%) was purchased from Thermo Scientific Acros, while methylammonium iodide (MAI) and formamidinium Iodide (FAI) were sourced from Greatcell Solar.

Solution preparation and sample fabrication processes were adapted from Klug *et al.*[3] and the details can be found below.

### 1.2 Solution Preparation

Three precursor solutions of $FA_{0.75}Cs_{0.25}SnI_3$, $FA_{0.75}Cs_{0.25}Sn_{0.5}Pb_{0.5}I_3$ and $FA_{0.6}MA_{0.4}Sn_{0.5}Pb_{0.5}I_3$ were prepared the day before thin-film deposition. In addition to the main precursor materials, 10 % molar excess of tin fluoride was added in all precursor solutions with respect to each of their tin content. A mixed solvent system of DMF:DMSO of 4:1 volumetric ratio was used to dissolve the precursor materials for all three solutions. A

solution of 1.2 M of $FA_{0.75}Cs_{0.25}SnI_3$ was prepared by dissolving 1341.07 mg of $SnI_2$, 464.31 mg of FAI, 233.82 mg of CsI and 56.4 mg of $SnF_2$ in 3 mL DMF:DMSO. A 1.2 M solution of $FA_{0.75}Cs_{0.25}Sn_{0.5}Pb_{0.5}I_3$ was prepared by dissolving 670.53 mg of $SnI_2$, 829.81 mg of $PbI_2$, 464.31 mg of FAI, 233.82 mg of CsI and 28.2 mg of $SnF_2$ in 3 mL of mixed DMF:DMSO. A 1.2 M of $FA_{0.6}MA_{0.4}Sn_{0.5}Pb_{0.5}I_3$ was prepared by dissolving 670.53 mg of $SnI_2$, 829.81 mg of $PbI_2$, 371.45 mg of FAI, 228.91 mg of MAI and 28.2 mg of $SnF_2$ in 3 mL of DMF:DMSO. Prior to spin coating, the perovskite solutions were filtered with a 0.2 μm PTFE syringe filter.

## 1.3 Sample Fabrication

Z-cut quartz disks (2 mm thick, 13 mm diameter) were used as substrates, which were cleaned with sequential sonication in acetone and isopropanol and treated with $O_2$-plasma for 5 minutes just before processing. Then, substrates were transferred to a nitrogen-filled glovebox, where the perovskite deposition took place. A one-step deposition method with antisolvent-quenching (anisole) was employed. 50 μL of each solution was dropped onto the substrate and spun statically with 4500 rpm with a 6 s ramp for 14 s. 100 μL of anisole was dispensed on the substrate 13 s after spinning begun. Right after the spin-coating program finished, $N_2$ gas flow was applied to the substrate for 10 s, during which the film darkened. The annealing step followed, for which the substrates were transferred onto a hotplate for 10 min. $FA_{0.75}Cs_{0.25}SnI_3$ and $FA_{0.75}Cs_{0.25}Sn_{0.5}Pb_{0.5}I_3$ were annealed at 120 °C, while $FA_{0.6}MA_{0.4}Sn_{0.5}Pb_{0.5}I_3$ was cured at 100 °C. After annealing, all samples were stored in a nitrogen-filled glovebox.

Top-view scanning electron microscope (SEM) was performed to examine the grain sizes of the two compositions. It was performed using a JEOL JSM-7100F FEG SEM operating at 10 kV accelerating voltage and 10 mm working distance. The top-view SEM of $FA_{0.75}Cs_{0.25}SnI_3$ is shown in **Figure S1.** Scanning electron miscroscope top-down images of (a, b) FA0.75Cs0.25SnI3 and (c, d) FA0.75Cs0.25Pb0.5Sn0.5I3 thin films.Figure S1(a) and (b), and that of $FA_{0.75}Cs_{0.25}Sn_{0.5}Pb_{0.5}I_3$ in Figure S1(c) and (d). We note $FA_{0.75}Cs_{0.25}SnI_3$ exhibits larger grain sizes than $FA_{0.75}Cs_{0.25}Sn_{0.5}Pb_{0.5}I_3$, which is in agreement with previous reports.[4,5]
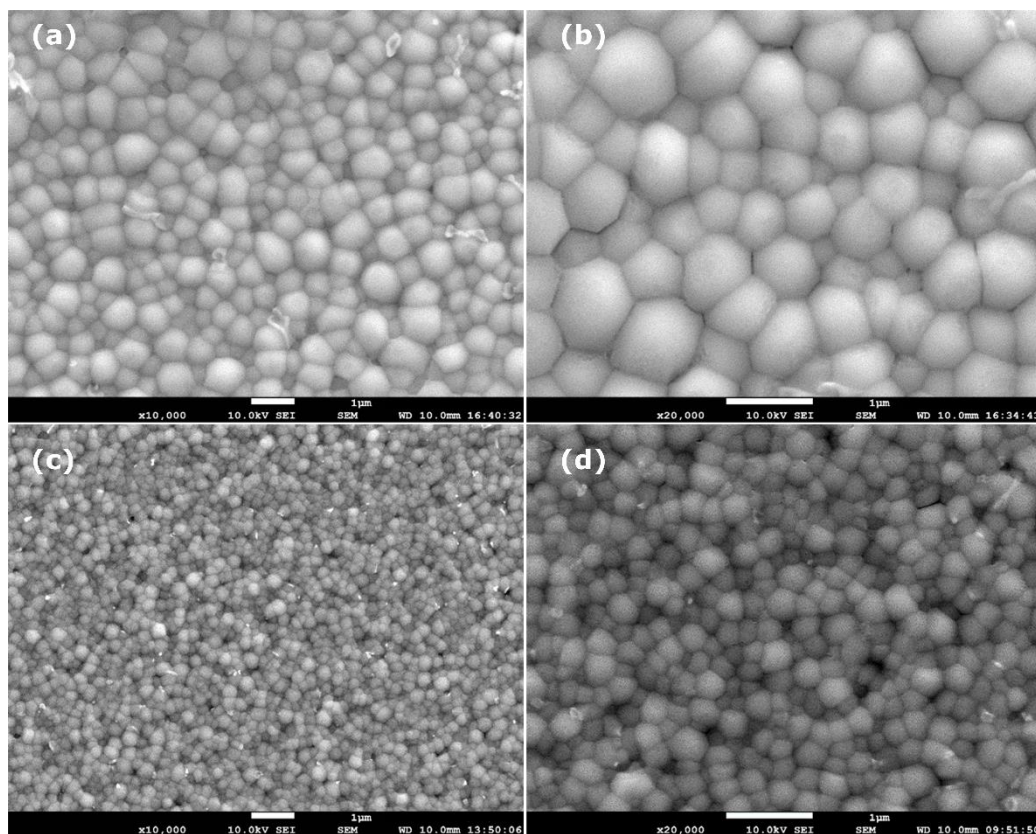
**Figure S1.** Scanning electron miscroscope top-down images of (a, b) $FA_{0.75}Cs_{0.25}SnI_3$ and (c, d) $FA_{0.75}Cs_{0.25}Pb_{0.5}Sn_{0.5}I_3$ thin films.

In order to avoid exposure to oxygen and moisture the samples were deposited and stored in a nitrogen filled glovebox. Before the measurements, the samples were transported in a sealed vacuum bag and were exposed to ambient air for < 1 min while being mounted into the vacuum chamber for OPTP and absorbance measurements, or while being mounted onto the sample holder for XRD measurements in ambient air.

## 2. Optical-pump THz-probe spectroscopy

Experimental details have been described in previous publications.[6,7] Briefly, the thin-film sample under consideration was photoexcited with pulses from an amplified ultrafast laser system (~ 35 fs pulse duration, 800 nm central wavelength Ti:Sapphire laser system from Spectra Physics: MaiTai – Ascend – Spitfire regenerative amplifier, frequency-doubled to 400 nm wavelength with a 1mm thick BBO crystal) at 5kHz repetition rate. The fluence of the pump pulse was controlled with a variable ND filter wheel. The relative time delays between pulses were set using optical delay stages, and the sample was illuminated with THz radiation generated with a tri-layer spintronic emitter (2 nm tungsten, 1.8 nm $Co_{40}Fe_{40}B_{20}$, 2 nm

platinum on quartz substrate)[8] after photoexcitation. The THz pulse was focused onto the sample using off-axis parabolic gold-coated mirrors, and then onto the detection crystal. The transmitted THz radiation was detected by electro-optic sampling in a 1 mm-thick (110)-ZnTe crystal with an 800 nm gate beam. The polarisation of the gate beam was measured using a quarter-wave plate, polarising beam splitter and a balanced photodiode detector. Every other THz pulse was blocked with an optical chopper while two consecutive pump pulses were blocked followed by two pump pulses being let through. THz transmission was detected using a lock-in technique implemented on a custom-made, field-programmable gate array-based data acquisition board. These measurements were conducted under vacuum, after exposing the samples to ambient air for discrete amounts of time at certain intervals, as indicated in the main text.

### 2.1. Charge-carrier recombination rate and mobility analysis

The terahertz transmission of the thin films was measured at the peak of the electric field of the THz pulse for different delays of the pump beam in the OPTP measurements, mapping the THz transmission as a function of time after photoexcitation. The pump pulse was delayed with respect to the gate beam with optical delay stages. The transmitted THz amplitude was calculated every two consecutive THz pulses (pump-on and pump-off), and the change in THz transmittance upon photoexcitation was calculated by comparing the two transmitted THz amplitudes with and without the pump pulse. The photoconductivity σ of the thin film sample is given by:[7]

$$\sigma = -\frac{\epsilon_0 c}{d}(1 + n_{substrate})\frac{\Delta T}{T} , \#(1)$$

where d is the thickness of the thin film, $n_{\text{substrate}} = 2.1$ is the refractive index of the substrate at THz frequencies,[9] $T$ is the transmitted THz radiation through the sample in the dark, $\Delta T$ is the difference in THz radiation between the photoexcited sample and the sample under no illumination. $\epsilon_0$ and $c$ are free space permittivity and speed of light, respectively.

However, the high dark conductivity of tin-only MHP means that Equation (1) no longer holds and has to be modified by adding a higher order term.[10,11] This results in:

$$\sigma = \left[\sigma_{\text{dark}} + \frac{\epsilon_0 c(n_{substrate} + 1)}{d}\right]\frac{\Delta T}{T}, \#(2)$$

where $\sigma_{dark}$ is the DC Drude conductivity of the film in the dark. $\sigma_{dark}$ was extracted from THz-TDS, as outlined in Section 4.1.

Photoconductivity decay transients can be used to extract the charge-carrier recombination dynamics. Briefly speaking, the decay of the charge-carrier population after photoexcitation *n(t)* can be described by the differential equation:[12]

$$\frac{dn}{dt} = -k_3 n^3 - k_2 n^2 - k_1 n, \#(3)$$

where $k_3, k_2$, and $k_1$ are the Auger, bimolecular and monomolecular recombination constants, respectively. However, the low excitation fluences used in our study, together with relatively large amounts of trap- or doping-assisted recombination in tin-iodide perovskites meant we could assume entirely monomolecular recombination of photoexcited charge carriers,

$$n(t) = A e^{k_1 t}. \#(4)$$

Equation (4) was fitted to the decay transients to extract the monomolecular recombination rates *k₁*. We present all measured photoconductivity decay transients for the tin-only and mixed tin-lead perovskite films in Figure S2 and Figure S3, respectively.
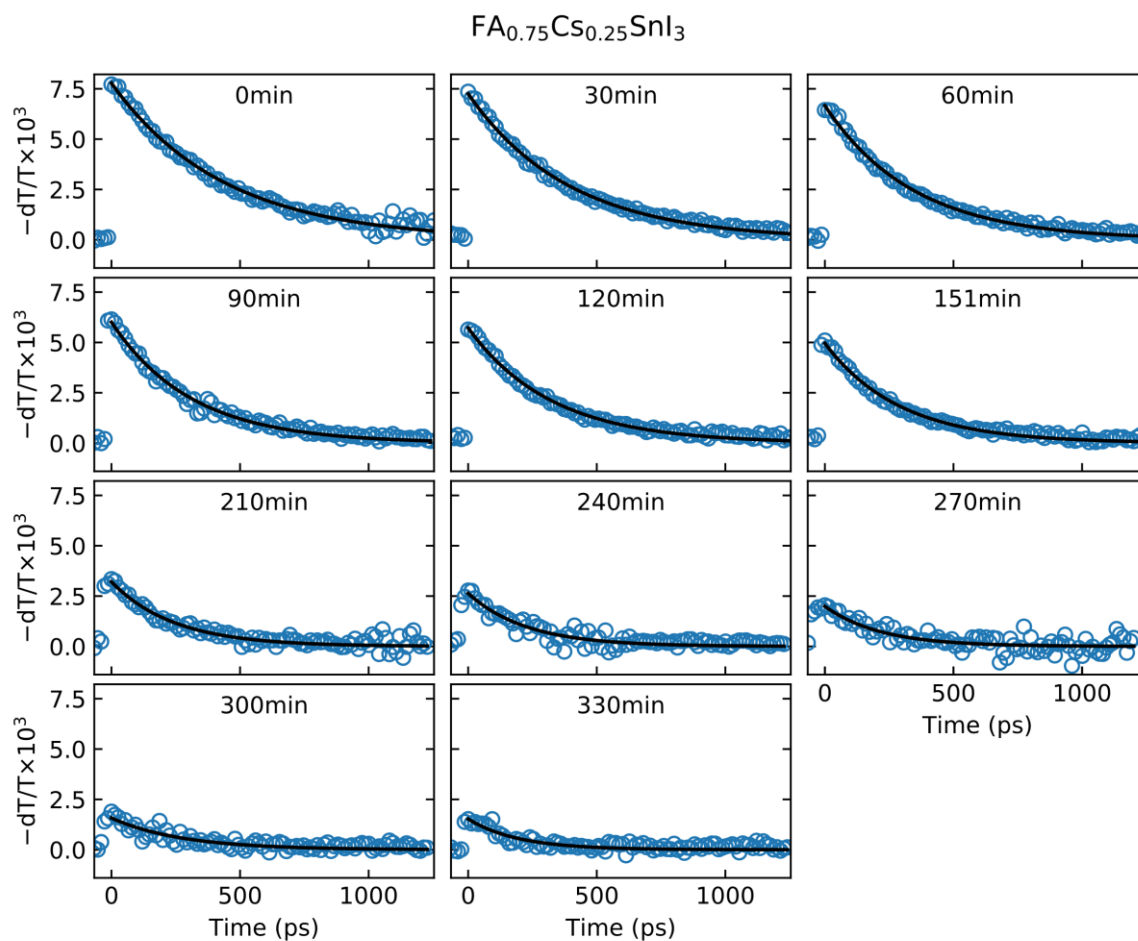
$FA_{0.75}Cs_{0.25}SnI_3$



**Figure S2.** Photoconductivity decay transients of a $FA_{0.75}Cs_{0.25}SnI_3$ thin film at different degradation times with monoexponential fits (black solid lines) shown on top of the data (empty hoops). The samples were excited with a 400 nm wavelength laser pulse with fluence of 3.6 $\mu Jcm^{-2}$
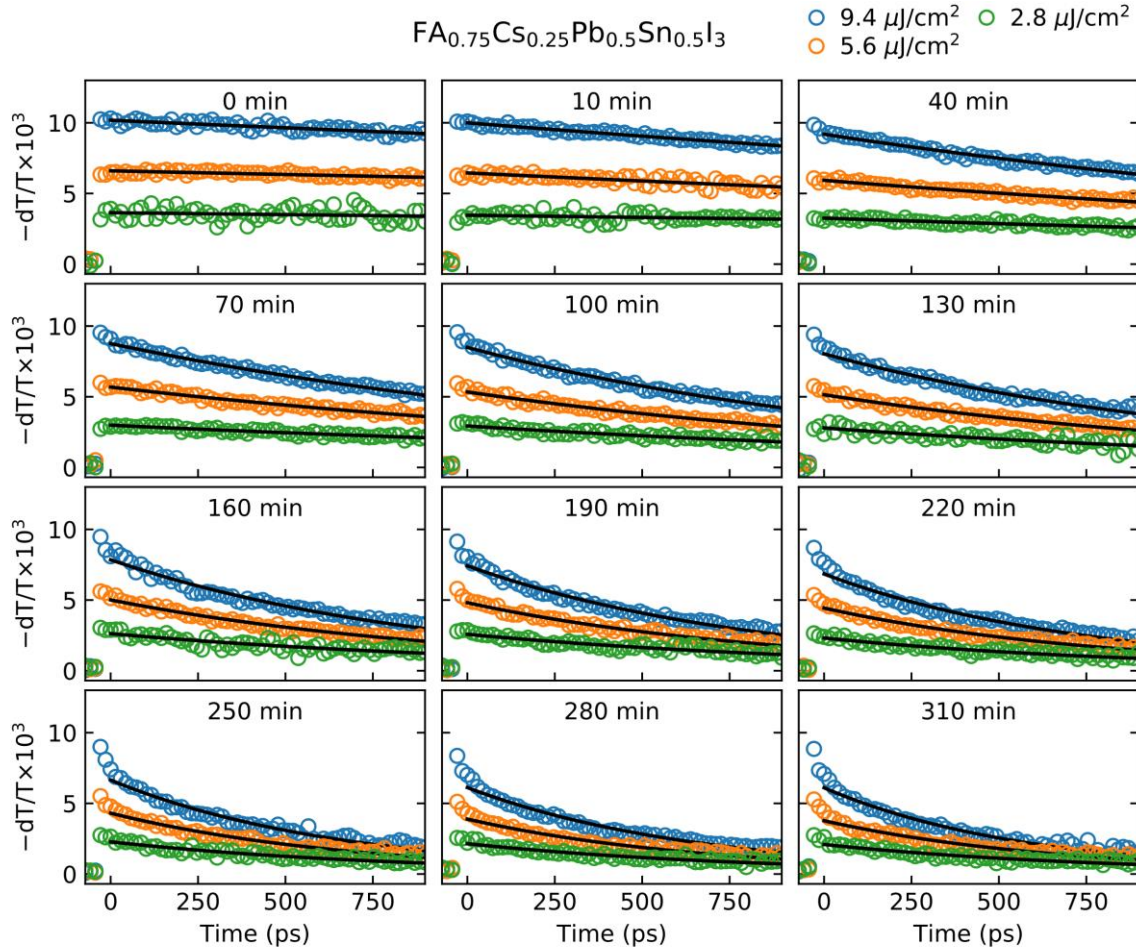
**Figure S3.** Photoconductivity decay transients of a $FA_{0.75}Cs_{0.25}Pb_{0.5}Sn_{0.5}I_3$ thin film measured for different fluences of the photoexcitation beam of 400 nm wavelength, as indicated in the legend. Transients are shown at different air exposure times indicated by the captions of sub-figures, with monoexponential fits in solid black line shown on top of the data (empty hoops).

These photoconductivity decay transients can be further examined to estimate the charge-carrier mobility, $\mu$, which is the sum of the electron and hole mobilities, from the expression

$$\sigma(t) = n(t)e\mu \quad \#(5)$$

where the conductivity $\sigma$ can be substituted from Equation (1). The charge-carrier density n at time = 0 can be estimated by:

$$n(t = 0) = \frac{E\lambda}{hcA_{eff}d}, \quad \#(6)$$

where $A_{eff}$ is the effective area of the overlap between the THz probe and pump pulse, $E$ is the energy of the photoexcitation pulse, $\lambda$ is the wavelength of the photoexcitation (400 nm), and $h$ is the Plank constant. Equation (5) and (6) can be used, along with Equation (1) or (2) for the lead-tin $FA_{0.75}Cs_{0.25}Pb_{0.5}Sn_{0.5}I_3$ and tin-only $FA_{0.75}Cs_{0.25}SnI_3$ respectively, with the peak onset value of the photoconductivity at time = 0 used to estimate the charge-carrier mobility. We assumed a perfect absorption of the pump pulse by the thin films and full conversion of each photon to a free electron-hole pair. These are reasonable assumptions because of the low exciton binding energy in these materials (resulting in high conversion of photons to free carriers) and the low bandgap energy of the materials compared to the excitation pulse photon energy (high absorption coefficient).

We note that the changes to the absorption coefficients with time under air exposure could in principle affect the extent to which the photoexcitation beam is absorbed, changing the extracted charge-carrier mobility. However, the lack of an overall decrease in the absorption strength at the excitation wavelength, as seen in **Error! Reference source not found.**(a) and (c) in the main text, implies that both the electronic and crystalline structure remain sufficiently unchanged over the ~ 15 hour air exposure, indicating that the changes observed in OPTP measurements presented in **Error! Reference source not found.** are predominantly caused by defect formation.

For mixed lead-tin $FA_{0.75}Cs_{0.25}Pb_{0.5}Sn_{0.5}I_3$ films the photoconductivity spectra were measured for three different fluences, so a linear fit between the $\Delta T/T$ and pump fluences was used to estimate the charge-carrier mobility, whereas for the tin-only $FA_{0.75}Cs_{0.25}SnI_3$ film photoconductivity spectra were measured only at one sufficiently low fluence.

Using the parameters extracted from the OPTP measurements, the charge-carrier diffusion length $L_D$ in the monomolecular recombination-dominated regime can be calculated using the charge-carrier recombination rate and mobility:[12]

$$L_{\mathrm{D}} = \sqrt{\frac{\mu k_{\mathrm{B}} T}{k_1 e}}, \#(7)$$

where $T$ is room temperature $T = 300$ K and $k_B$ is Boltzmann constant. The charge-carrier diffusion length can be used as the figure of merit for materials for PV applications, since it is an estimation of how far charge carriers can travel in the device without any electric field bias, giving an indication of the thickness of the absorption layer required to obtain efficient charge-carrier extraction. Calculated diffusion lengths for both films are presented in Figure S4 for various degradation times.
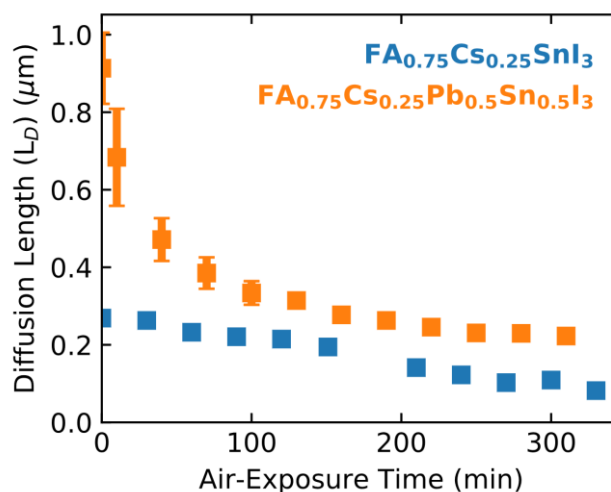


**Figure S4.** Charge-carrier diffusion lengths at different ambient air exposure times, derived from OPTP measurements of charge-carrier mobilities and recombination rates for thin films of tin-only $FA_{0.75}Cs_{0.25}SnI_3$ and mixed lead-tin $FA_{0.75}Cs_{0.25}Pb_{0.5}Sn_{0.5}I_3$ perovskites.

We further examined whether any degradation was induced through the laser illumination during measurements. For each of our OPTP transient recorded, we gathered three consecutive measurements of which the average is shown in the main manuscript. Below, we present all three transients for the initially pristine $FA_{0.75}Cs_{0.25}Pb_{0.5}Sn_{0.5}I_3$ and $FA_{0.75}Cs_{0.25}SnI_3$ thin films (air-exposure time = 0) in Figure S5. The optoelectronic properties of the MHPs degrade fastest at the beginning of the air exposure, as can be seen from Figure 1 in the main text, so any possible degradation from laser illumination should be most visible from the Figure S5, however, no systematic change or degradation is evident. We therefore conclude that there is no significant degradation from laser illumination during these measurements under vacuum. We further note that during air exposure in between these scans being taken,

no laser illumination was present. Therefore, the changes observed were solely the result of moist ambient air exposure.
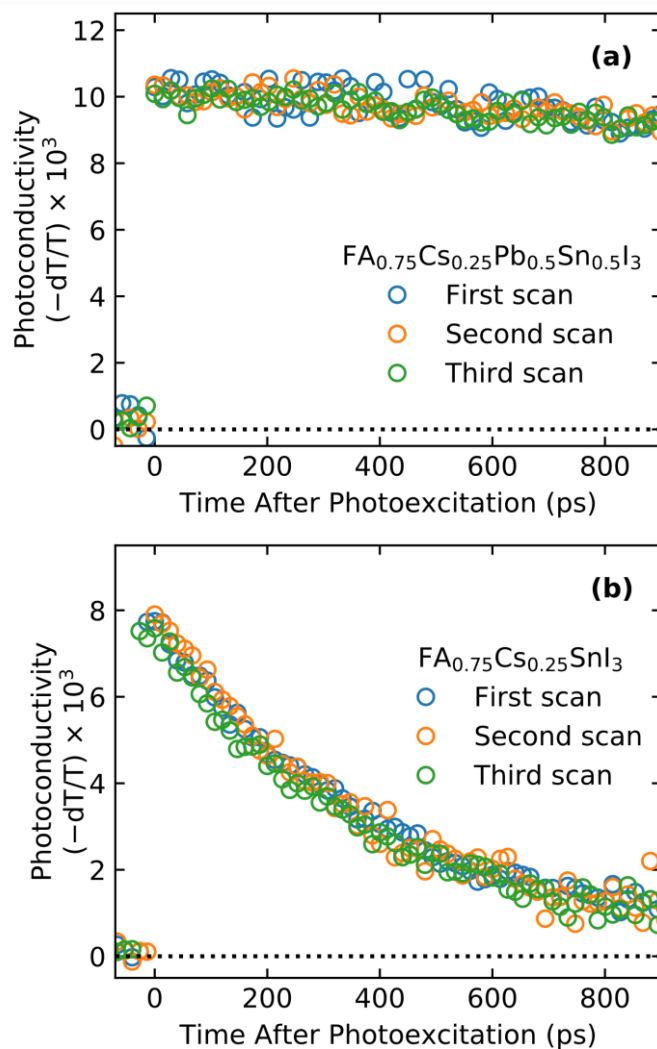


**Figure S5.** Consecutive photoconductivity decay transients recorded for (a) $FA_{0.75}Cs_{0.25}Pb_{0.5}Sn_{0.5}I_3$ and (b) $FA_{0.75}Cs_{0.25}SnI_3$ thin films at 0 air-exposure time. The samples were excited with 400 nm wavelength laser pulses with fluence of 3.6 μJ/cm$^2$ for (a) and 9.4 μJ/cm$^2$ for (b).

## 3. Absorption measurements

Fourier-transform infrared (FTIR) spectroscopy was employed to measure the absorption spectra of the thin films. A Bruker Vertex 80v FTIR spectrometer with a silicon detector and CaF$_2$ beamsplitter was used in transmission/reflection geometry, using vacuum and a silver mirror as references for transmission and reflection, respectively. Absorbance was calculated

as

$$\text{Absorbance} = -\ln\left(\frac{T}{1-R}\right), \#(8)$$

where $T$ is the transmittance and $R$ is the reflectance of the thin samples, referenced to the vacuum transmission and reflection of a silver mirror. We performed the measurements in vacuum, at discrete air exposure times. The measurements were carried out over ~ 15 hours of air exposure (30 minutes of air exposure between measurements, 30 scans in total, including the pristine state).

### 3.1. Elliott Fitting

The absorbance spectra were fitted with an expression derived from Elliott Theory describing the absorption of a semiconductor in the presence of Coulomb correlations,[13] similar to previous reports.[13–15] This fitting allowed us to attribute the changes in the absorbance observed during degradation to both the blueshift of bandgap arising from the Burstein-Moss effect, and the decrease of the exciton binding energy caused by screening resulting from unintentional electrical doping.

The absorption given by the Elliott model is:

$$\alpha(E) = \alpha_X(E) + \alpha_C(E), \#(9)$$

where $\alpha_X$ is the exciton and $\alpha_C$ is the continuum contribution to the absorbance. The exciton contribution is given by:

$$\alpha_X(E) = \frac{b_0}{E} \sum_{n=1}^{\infty} \frac{4\pi E_b^{\frac{3}{2}}}{n^3} \delta\left(E - \left[E_g - \frac{E_b}{n^2}\right]\right), \#(10)$$

where the electric dipole transition matrix element between the conduction and the valence bands is incorporated in the proportionality constant $b_0$. $E_b$ is the exciton binding energy, $E_g$ is the bandgap, and $n$ is the quantum number of the exciton. The electron-hole continuum contribution is given by:

$$\alpha_C(E) = \frac{b_0}{E} \left[\frac{2\pi\sqrt{\frac{E_b}{E - E_g}}}{1 - \exp\left(-2\pi\sqrt{\frac{E_b}{E - E_g}}\right)}\right] c_0^{-1} \text{JDoS}(E), \#(11)$$

11

where the joint density of states $\text{JDoS} = \frac{c_0}{1-b(E-E_g)}\sqrt{E-E_g}$ for $E > E_g$, and $0$ otherwise, where b is the band non-parabolicity factor,[16] and $c_0 = \frac{2}{(2\pi)^2}\left(\frac{2\mu}{\hbar^2}\right)^{3/2}$, where $\mu$ is the reduced effective mass of the electron-hole system. A Gaussian broadening was also introduced by convolving $\alpha(E)$ with a normal distribution $N(0,\Gamma^2)$.

For the lead-tin $FA_{0.75}Cs_{0.25}Pb_{0.5}Sn_{0.5}I_3$ and tin-only $FA_{0.75}Cs_{0.25}SnI_3$ perovskites under consideration in our study, the absorbance in the pristine state was fitted by the Elliot formula (combining equations 9-11), varying all the parameters to achieve the best fit (using the Nelder-Mead method). Subsequently, most of the fitting parameters were fixed, and only the bandgap $E_g$ and the exciton binding energy $E_b$ were allowed to be varied as free parameters to optimize the fitting function for different exposure times. The fitted parameters for the pristine (0 exposure time in ambient air) are given in

Table **1**. The fits to the absorbance data are presented in Figure S6.

We note that Elliott theory may not fully accurately capture the shape of the absorption spectrum far above the bandgap,[15] owing to band non-parabolicity, the electronic dipole matrix element varying with energy, transitions to higher-lying states, and Fermi-level shifting owing to doping, all of which are not accounted for by this theory. However, when limited to fits near the absorption onset, extracted values of $E_g$ and $E_b$ will still be useful to reveal changes in absorption onset and electron-hole Coulomb attraction parameters with increasing air exposure time.

|  | Tin-only | Mixed lead-tin |
|---|---|---|
| $E_b$ (eV) | 0.0205 | 0.0201 |
| $E_g$ (eV) | 1.3987 | 1.3562 |
| Amplitude | 1.4375 | 1.0587 |
| $b$ (eV$^{-1}$) | 1.6045 | 1.6305 |
| $\Gamma$ (eV) | 0.0484 | 0.0478 |
| Fitting range (eV) | 1.25-1.49 | 1.21-1.435 |

**Table 1.** Parameters extracted from Elliott fits to the absorption spectra of tin-only $FA_{0.75}Cs_{0.25}SnI_3$ and mixed lead-tin $FA_{0.75}Cs_{0.25}Pb_{0.5}Sn_{0.5}I_3$ perovskite thin films in their pristine state (prior to air exposure), and the range of photon energies used to fit the data. These results were used for subsequent fitting of the absorption spectra of air-degraded samples, varying only the exciton binding energy and bandgap to optimize the fits, leaving other fit parameters unchanged.
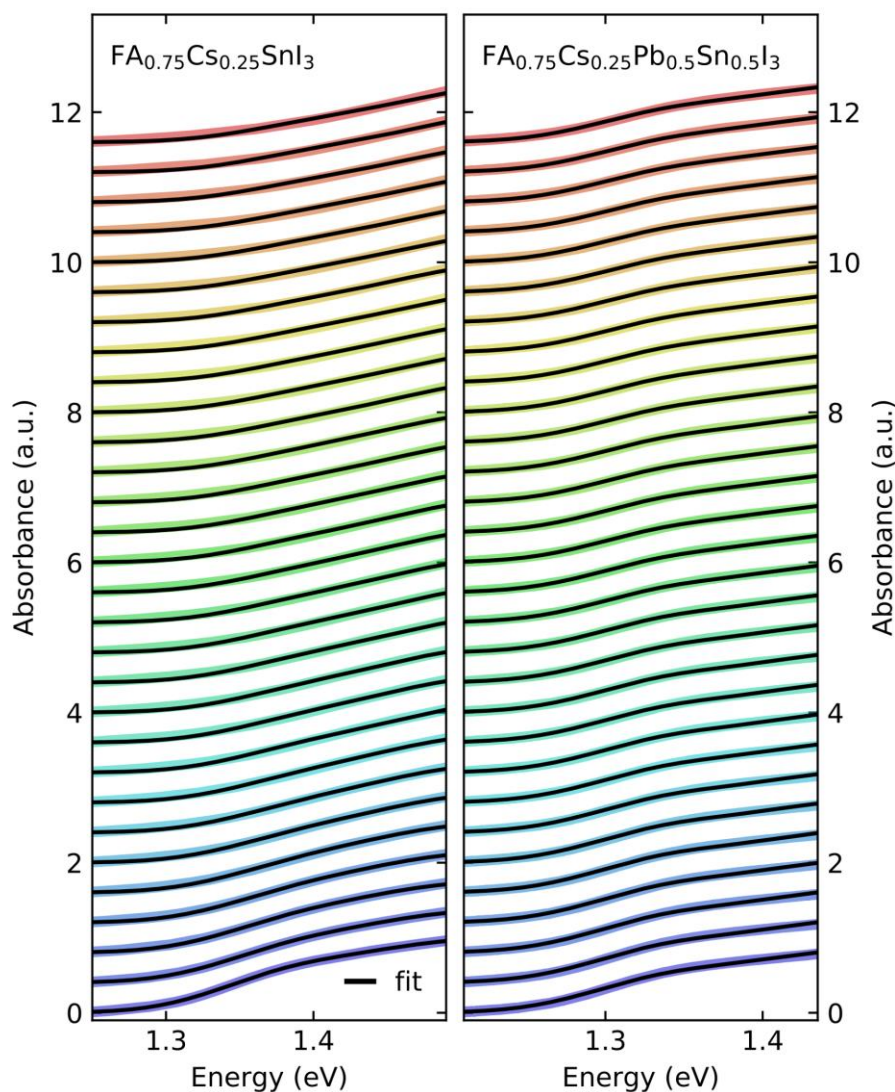


**Figure S6.** Elliott fits (black lines) to the absorption spectra (colored lines) of tin-only $FA_{0.75}Cs_{0.25}SnI_3$ and mixed lead-tin $FA_{0.75}Cs_{0.25}Pb_{0.5}Sn_{0.5}I_3$ perovskites for the first ~ 15 hours of ambient air exposure.

We further ascertained whether the absorption of the excitation pump pulse changed as a result of air-induced degradation by examining the absorbance spectra down to the excitation pump wavelength of 400 nm. As an example, **Figure S7** shows the absorbance spectrum of the $FA_{0.75}Cs_{0.25}SnI_3$ thin film, which shows stronger air-degradation effects than the $FA_{0.75}Cs_{0.25}Pb_{0.5}Sn_{0.5}I_3$ sample. The absorbance at 400 nm falls from slightly above OD4 to slightly below OD4 with air-induced degradation, which would leave the overall fraction of charge-carriers absorbed by the pulse virtually unchanged.
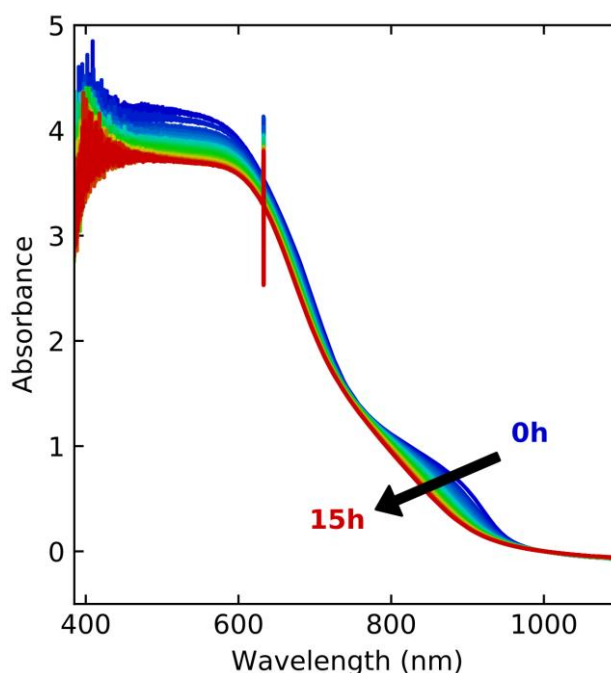


**Figure S7.** Absorbance spectra of a $FA_{0.75}Cs_{0.25}Pb_{0.5}Sn_{0.5}I_3$ thin film sample recorded at different ambient air-exposure times.

## 4. Terahertz time-domain spectroscopy

The same setup as the one described for OPTP in Section 2 was used for terahertz time-domain spectroscopy (THz-TDS), with the pump pulse blocked. In this measurement, the THz pulse delay was varied with respect to the stationary gate beam, to obtain the time-domain shape of the THz electric field pulse. These measurements were performed under vacuum, at discrete air exposure times, with samples exposed to air at interims to induce degradation as indicated.

### 4.1. Dark conductivity analysis

The measured time-domain transmission through the thin film was Fourier transformed into a frequency space, $\tilde{T}_{sample}$, and compared to the transmission through the bare substrate $\tilde{T}_{substrate}$. The following formula was then used to calculate the dark conductivity spectrum of the thin film:[11,17–19]

$$\tilde{\sigma}_{\text{dark}} = \frac{\tilde{T}_{\text{substrate}} - \tilde{T}_{\text{sample}}}{\tilde{T}_{\text{sample}}} \frac{\epsilon_0 c (1 + n_{\text{substrate}})}{d}, \#(12)$$

where $n_{\text{substrate}}$ is the refractive index of the substrate (2.1 in z-cut quartz substrates used for our study[9]), $d$ is the thickness of the thin film sample, and $c$ and $\epsilon_0$ are the speed of light in free space and permittivity of free space, respectively.

The thickness of the samples was measured using Dektak 150 Surface profiler. The measured thicknesses are given in Table 2.

| Sample | Thickness |
|---|---|
| $FA_{0.75}Cs_{0.25}SnI_3$ | $310 \pm 13$ nm |
| $FA_{0.75}Cs_{0.25}Pb_{0.5}Sn_{0.5}I_3$ | $430 \pm 50$ nm |
| $FA_{0.6}MA_{0.4}Pb_{0.5}Sn_{0.5}I_3$ | $310 \pm 60$ nm |

**Table 2.** Thicknesses of the thin film samples used for dark conductivity measurements.

Equation (12) assumes the same thickness for the reference substrate and the sample substrate. We corrected for any actual difference in thickness by measuring the thicknesses of the substrates after THz measurements, and applied a phase correction of $e^{i\omega\Delta n\Delta t/c}$, where $\omega$ is the angular frequency of the THz probe, $\Delta n$ is the difference in refractive index between air and substrate (1.1 in our study[9]), and $\Delta t$ is the difference in the thicknesses of the substrates, measured with a micrometer screw with resolution of 1 µm.

### 4.2. Background doping density determination

We estimated the background hole doping density in the tin-only MHP using the evolution of dark conductivity spectrum and the charge-carrier mobility from Figure 3 and 1 respectively. We assume that the hole mobility is the same as the electron mobility from similar effective masses of electrons and holes,[20,21] so use $\mu_h = \mu_{sum}/2$. We also employed the relation $\sigma = ep_0\mu_h$, where $e$ is the elementary charge, and $p_0$ the background hole density. The dark conductivity contribution from the background holes was estimated by averaging the dark conductivity in the low frequency region (0.4 – 0.7 THz), where the phonon contribution from optical modes is insignificant. The detection limit of the background doping density was

estimated from the signal to noise level of our measurement and the relation $\sigma = ep_0\mu_h$, obtaining $p_0^{lim} \sim 10^{18}$ cm$^{-3}$ as our detection limit.

## 5. X-ray diffraction

X-ray diffraction (XRD) measurements were performed for samples held in ambient air using thin films deposited on quartz substrates, either continuously over ~ 12 hours (24 scans were performed consecutively, and each scan lasted 30 minutes, the XRD patterns are shown in Figure S8) or at 0, 24, 48 and 72 hours of discrete degradation times in air (as shown in Figure S9). Each of the data sets presented in Figure 4 in the main text is therefore from two different measurements on samples from two different batches. A PANalytical X'Pert powder diffractometer with a Cu-K$_{\alpha 1}$ source was employed for these XRD measurements, across a $2\theta$ range between 11 ° and 38 °. A constant angular offset was applied as a sample tilt correction using the quartz substrate reference peak at $2\theta = 16.43$ °.[10]

As mentioned in Figure 4 of the main text, the FA$_{0.75}$Cs$_{0.25}$Pb$_{0.5}$Sn$_{0.5}$I$_3$ thin film sample exhibited a decrease in diffraction angle $2\theta$ as it degrades. However, as can be seen from Figure S8 and Figure S9, the FA$_{0.6}$MA$_{0.4}$Pb$_{0.5}$Sn$_{0.5}$I$_3$ thin film did not exhibit such shift, and so we attribute such lattice contraction to degradation effects related to the A-cation composition.
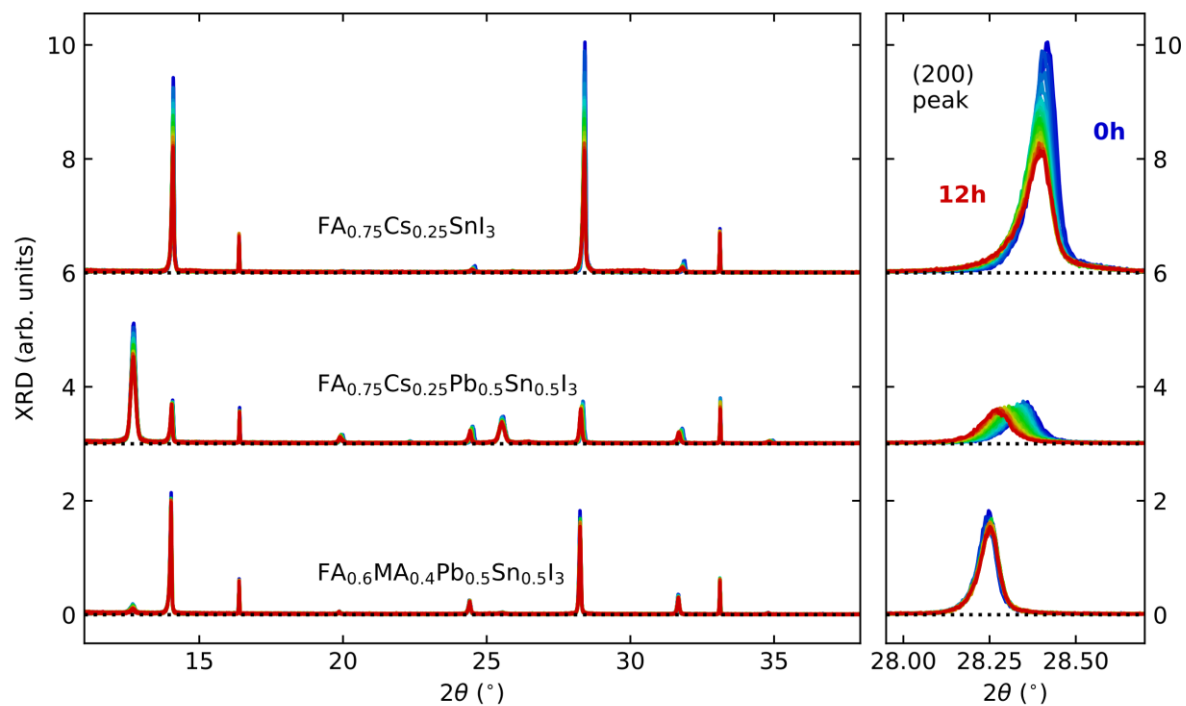
**Figure S8.** Continuously recorded XRD patterns over ~ 12 hours of ambient air exposure of thin films of $FA_{0.75}Cs_{0.25}SnI_3$, $FA_{0.75}Cs_{0.25}Pb_{0.5}Sn_{0.5}I_3$, and $FA_{0.6}MA_{0.4}Pb_{0.5}Sn_{0.5}I_3$ perovskite. The right-hand panel is a zoomed-in view of the (200) peak.

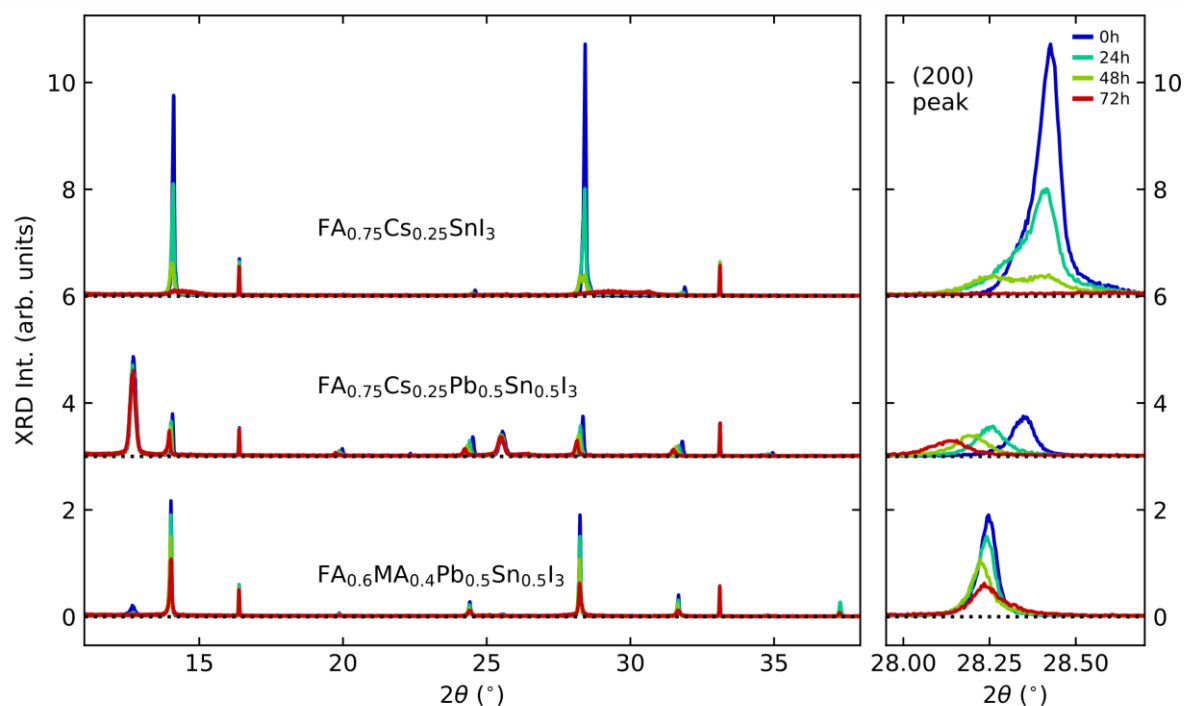**Figure S9.** XRD patterns over 72 hours of ambient air exposure of thin films of $FA_{0.75}Cs_{0.25}SnI_3$, $FA_{0.75}Cs_{0.25}Pb_{0.5}Sn_{0.5}I_3$, and $FA_{0.6}MA_{0.4}Pb_{0.5}Sn_{0.5}I_3$ perovskite. The right-hand panel is a zoomed- in view of the (200) peak.

## 6. Discussion on vacancy-ordered double perovskite

In agreement with previous reports,[22–24] we suggest that vacancy-ordered double perovskite is a possible degradation product of tin-only $FA_{0.75}Cs_{0.25}SnI_3$ in ambient air, based on the dark conductivity measurement shown in Figure 3 of the main text and XRD measurement shown in Figure 4 of the main text. The phonon peaks evident in the dark conductivity measurements at prolonged degradation times for $FA_{0.75}Cs_{0.25}SnI_3$ agree closely with those of previously reported transverse optical phonon modes of $Cs_2SnI_6$.[25] The corresponding phonon modes of $(FA_{0.75}Cs_{0.25})_2SnI_6$ or $FA_2SnI_6$ have not been reported in the literature so far. The lowest frequency transverse optical modes that we observe have been identified previously to be a lattice vibration involving the A-cation, which would imply that the frequency is expected to vary with different A-cation composition; from the difference in mass between $FA^+$ and $Cs^+$ we would expect a notable difference in phonon mode frequencies, which however appears absent here. We suggest that the $Cs^+$ submode could possess a higher cross section for interaction with respect to the THz excitation compared to $FA^+$, however, modelling of THz interactions with such modes in real-world structures would require calculations beyond the scope of this study.

18

The XRD patterns presented in Figure 4 of the main text provide further evidence to the formation of such vacancy-ordered double perovskite. An appearance of the broad XRD peak at a higher angle is attributed to this degradation product. The lattice parameter of the vacancy-ordered double perovskite is expected to be lower than for the pristine $FA_{0.75}Cs_{0.25}SnI_3$, since the 4+ oxidation state of tin would lead to an enhanced Coulomb attraction with the rest of the structure.[26] We would therefore also expect a mismatch in lattice parameters between the MHP and double perovskite domains, causing strains, in accordance with the broad peaks that we observe. This broadening, however, may also arise from the presence of very small crystalline domains of the vacancy-ordered double perovskites.

References

[1]     T. Leijtens, R. Prasanna, K. A. Bush, G. E. Eperon, J. A. Raiford, A. Gold-Parker, E. J. Wolf, S. A. Swifter, C. C. Boyd, H.-P. Wang, M. F. Toney, S. F. Bent, M. D. McGehee, *Sustain. Energy Fuels* **2018**, *2*, 2450.

[2]     D. Zhao, Y. Yu, C. Wang, W. Liao, N. Shrestha, C. R. Grice, A. J. Cimaroli, L. Guan, R. J. Ellingson, K. Zhu, X. Zhao, R.-G. Xiong, Y. Yan, *Nat. Energy* **2017**, *2*, 17018.

[3]     M. T. Klug, R. L. Milot, J. B. Patel, T. Green, H. C. Sansom, M. D. Farrar, A. J. Ramadan, S. Martani, Z. Wang, B. Wenger, J. M. Ball, L. Langshaw, A. Petrozza, M. B. Johnston, L. M. Herz, H. J. Snaith, *Energy Environ. Sci.* **2020**, *13*, 1776.

[4]     G. E. Eperon, T. Leijtens, K. A. Bush, R. Prasanna, T. Green, J. T.-W. Wang, D. P. McMeekin, G. Volonakis, R. L. Milot, R. May, A. Palmstrom, D. J. Slotcavage, R. A. Belisle, J. B. Patel, E. S. Parrott, R. J. Sutton, W. Ma, F. Moghadam, B. Conings, A. Babayigit, H.-G. Boyen, S. Bent, F. Giustino, L. M. Herz, M. B. Johnston, M. D. McGehee, H. J. Snaith, *Science* **2016**, *354*, 861.

[5]     R. L. Milot, M. T. Klug, C. L. Davies, Z. Wang, H. Kraus, H. J. Snaith, M. B. Johnston, L. M. Herz, *Adv. Mater.* **2018**, *30*, 1804506.

[6]     P. Tiwana, P. Parkinson, M. B. Johnston, H. J. Snaith, L. M. Herz, *J. Phys. Chem. C* **2009**, *114*, 1365.

[7]     C. Wehrenfennig, M. Liu, H. J. Snaith, M. B. Johnston, L. M. Herz, *Energy Environ. Sci.* **2014**, *7*, 2269.

[8]     T. Seifert, S. Jaiswal, U. Martens, J. Hannegan, L. Braun, P. Maldonado, F. Freimuth, A. Kronenberg, J. Henrizi, I. Radu, E. Beaurepaire, Y. Mokrousov, P. M. Oppeneer, M. Jourdan, G. Jakob, D. Turchinovich, L. M. Hayden, M. Wolf, M. Münzenberg, M. Kläui, T. Kampfrath, *Nat. Photonics* **2016**, *10*, 483.

[9]  C. L. Davies, J. B. Patel, C. Q. Xia, L. M. Herz, M. B. Johnston, *J. Infrared, Millimeter, Terahertz Waves* **2018**, *39*, 1236.

[10]  K. J. Savill, A. M. Ulatowski, M. D. Farrar, M. B. Johnston, H. J. Snaith, L. M. Herz, *Adv. Funct. Mater.* **2020**, *30*, 2005594.

[11]  A. M. Ulatowski, L. M. Herz, M. B. Johnston, *J. Infrared, Millimeter, Terahertz Waves* **2020**, *41*, 1431.

[12]  L. M. Herz, *Annu. Rev. Phys. Chem.* **2016**, *67*, 65.

[13]  R. J. Elliott, *Phys. Rev.* **1957**, *108*, 1384.

[14]  A. D. Wright, G. Volonakis, J. Borchert, C. L. Davies, F. Giustino, M. B. Johnston, L. M. Herz, *Nat. Mater.* **2020**, *19*, 1201.

[15]  C. L. Davies, M. R. Filip, J. B. Patel, T. W. Crothers, C. Verdi, A. D. Wright, R. L. Milot, F. Giustino, M. B. Johnston, L. M. Herz, *Nat. Commun.* **2018**, *9*, 293.

[16]  J. M. Ball, L. Buizza, H. C. Sansom, M. D. Farrar, M. T. Klug, J. Borchert, J. Patel, L. M. Herz, M. B. Johnston, H. J. Snaith, *ACS Energy Lett.* **2019**, *4*, 2748.

[17]  M. Tinkham, *Phys. Rev.* **1956**, *104*, 845.

[18]  R. E. Glover, M. Tinkham, *Phys. Rev.* **1957**, *108*, 243.

[19]  A. M. Ulatowski, M. D. Farrar, H. J. Snaith, M. B. Johnston, L. M. Herz, *ACS Photonics* **2021**, *8*, 2509.

[20]  S. Poncé, M. Schlipf, F. Giustino, *ACS Energy Lett.* **2019**, *4*, 456.

[21]  P. Umari, E. Mosconi, F. De Angelis, *Sci. Rep.* **2014**, *4*, DOI 10.1038/srep04467.

[22]  X. Qiu, B. Cao, S. Yuan, X. Chen, Z. Qiu, Y. Jiang, Q. Ye, H. Wang, H. Zeng, J. Liu, M. G. Kanatzidis, *Sol. Energy Mater. Sol. Cells* **2017**, *159*, 227.

[23]  L. Lanzetta, T. Webb, N. Zibouche, X. Liang, D. Ding, G. Min, R. J. E. Westbrook, B. Gaggio, T. J. Macdonald, M. S. Islam, S. A. Haque, *Nat. Commun.* **2021**, *12*, 2853.

[24]  A. G. Kontos, A. Kaltzoglou, E. Siranidi, D. Palles, G. K. Angeli, M. K. Arfanis, V. Psycharis, Y. S. Raptis, E. I. Kamitsos, P. N. Trikalitis, C. C. Stoumpos, M. G. Kanatzidis, P. Falaras, *Inorg. Chem.* **2017**, *56*, 84.

[25]  A. Kaltzoglou, M. Antoniadou, A. G. Kontos, C. C. Stoumpos, D. Perganti, E. Siranidi, V. Raptis, K. Trohidou, V. Psycharis, M. G. Kanatzidis, P. Falaras, *J. Phys. Chem. C* **2016**, *120*, 11777.

[26]  Y. El Ajjouri, F. Locardi, M. C. Gélvez-Rueda, M. Prato, M. Sessolo, M. Ferretti, F. C. Grozema, F. Palazon, H. J. Bolink, *Energy Technol.* **2020**, *8*, 1900788.